Niobium Bearing Structural Steels
Edited by: Steven G. Jansto and Jitendra Patel
TMS (The Minerals, Metals & Materials Society), 2010

INFLUENCE OF NB ON THE DEVELOPMENT OF STAINLESS STEEL LONG PRODUCTS

Marc Mantel, Nicolas Renaudot
Centre de Recherches, UGITECH, Schmolz + Bickenbach group
Avenue Paul Girod, 73403 Ugine, France
Nicolas Meyer, Muriel Veron
SIMAP INPGrenoble-CNRS-UJF, Groupe Physique du Métal,
BP 75, 38402 Saint Martin d'Hères – France
Olivier Geoffroy
Laboratoire Louis Néel, CNRS, BP 166, 38042 Grenoble - France

Keywords: 17%Cr Stainless Steel, Nb Stabilization, Magnetic Losses, Welding Filler

Abstract

Usually niobium is added in ferritic stainless steels to avoid chromium carbides precipitation and then to improve corrosion resistance and to avoid embrittlement. This work shows that niobium can also be used in ferritic stainless steels long products to improve soft magnetic properties for actuators in the automotive industry or to improve the properties of a welding filler wire for the exhaust line of a car.

The first example concerns stainless steels bars for the market of electromagnetic injection. Improving response-time of fuel injection valves is a great challenge for automotive industry in order to enhance car engine efficiency and to limit noxious gas emission. It is shown that low niobium stabilization makes recrystallization nucleation much faster and then prevents incomplete recrystallization. This leads to soft magnetic properties that make 17%CrNb ferritic stainless steels a very interesting solution for actuation. The second example concerns a new welding filler wire 430LNb for the exhaust line that combines corrosion resistance to salt attack, cyclic oxidation and thermal fatigue resistance of the weld.

Introduction

The aim of this paper is to present two cases in which the addition of niobium has changed significantly metallurgical properties of stainless steel. Then we will show how these improvements have been used to develop new stainless steels long product and special applications for the automotive industry.

Improving response-time of fuel injection valves is a great challenge for the automotive industry because it constitutes a direct way to enhance car engine efficiency and to limit noxious gas emission. For an electromagnetic injector, the response-time depends particularly on the

magnetic properties of the actuator. 17% Cr ferritic stainless steels is a very interesting solution for actuation because it combines a good corrosion resistance with rather soft magnetic properties [1]. The aim of this project is to find the optimum adjustment of microstructure to lower magnetic losses under dynamic excitation.

To understand the relationship between the microstructure and magnetic losses, different microstructural states were generated by varying the annealing conditions that led to either recovery or to recrystallization. Low level niobium stabilization was also considered in order to widen the range of microstructures formed, since niobium is an important addition element in the design of corrosion resistant stainless steels [2]. This first part mainly focuses on the understanding of the annealing phenomena kinetics and the microstructure evolution. Interaction between magnetic losses and microstructure is illustrated on the Nb stabilized grade to demonstrate the interest of such an approach.

The second part of this paper concerns a new welding filler wire 430LNb for the exhaust line that combines corrosion resistance to salt attack, cyclic oxidation and thermal fatigue resistance of the weld. Indeed, the increasing use of stabilized ferritic stainless steel sheets (AISI 409, 439, 436 and 441) in automotive exhaust systems has led to develop a new stabilized ferritic welding wire instead of the austenitic 308LSi grade.

This ferritic stainless steel welding wire has been developed to meet the requirements associated with the increasing use of AISI 441, for which the 409Cb filler wire cannot be used, due to the trend towards higher temperatures in the upstream part of exhaust systems to improve the efficiency of catalytic converters.

In this paper it is shown that the new wire Exhaust™ F1 has weldability and service properties equal to, and in some cases better than, those of the 308LSi and 307Si austenitic grades, for the welding of ferritic grades as well as for heterogeneous welding (assemblies containing carbon steels, ferritic stainless steels and/or austenitic stainless steels). Weldability was evaluated by joining the different sheets most commonly encountered on an exhaust line. The functional properties were determined by measuring the corrosion and oxidation resistance, together with the thermal fatigue strength. This was done with the aid of specially developed tests, which are briefly described below. Productivity of Exhaust™ F1 compared to 308LSi solid wire (SW) and 430LNb Metal Cored Wire (MCW) is also described as well as the results of industrial welding operations on real exhaust system components using Exhaust™ F1 wire.

Nb in Stainless Steel for Magnetic Applications

Materials and Experimental Procedure

Initial State

Table 1 reports the chemical composition of the two industrial casts melted by UGITECH and considered in this work. The materials were received in the form of wires of diameter 12.5mm, obtained by hot rod rolling around 1200°C. To start from fully ferritic states for both grades, an additional heat treatment around 850°C was performed on 430 to remove the martensite formed during cooling from 1200°C. In the initial state, both grades are fully ferritic and have the same

hardness (HV1 = 145). However, a major difference concerning precipitation is seen in Figure 1: 430Nb exhibits homogeneous precipitation of Nb(C,N) whereas, in 430, the precipitates identified as Cr_2N and $M_{23}C_6$ are located in grain boundaries and in bands parallel to the rolling direction.

Table 1. Chemical composition analysis and stabilization level
ΔNb [wt. %]; the stoichiometric relation for ΔNb is given in [2].

grade (AISI)	C	N	Cr	Nb	Mn	Si	ΔNb
430	0,017	0,028	16,083	0,004	0,405	0,345	–
430Nb	0,015	0,012	16,284	0,27	0,324	0,35	0,076

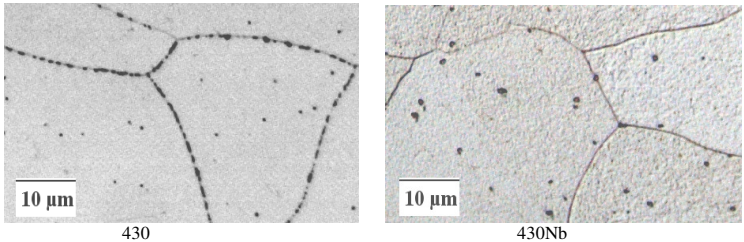

430 430Nb

Figure 1. Optical micrographs in the initial state after etching using Villela reagent. 430 exhibits intense intergranular precipitation whereas 430Nb presents weak homogeneous precipitation.

Laboratory Thermomechanical Treatments

From the start, the two grades received exactly the same thermomechanical treatments. First, a 20% nominal strain in tension was performed at room temperature and at 3.10^{-4} s^{-1} strain rate. After this cold deformation and heat treatments were performed in a salt bath at two temperatures (750°C and 850°C) for different times from 30s to 1h and were followed by quenching in water. The accurate thermal analysis curve at the center of the rod was measured with a thermocouple inserted in a hole drilled along the rod axis and revealed that the salt bath temperature is reached to within 10°C after 40s. The temperature versus time relationship T(t) has been determined by fit on experimental thermal analysis data but, is not detailed here for conciseness reasons.

Longer heat treatments at 850°C, from 2h to 16h, were performed in a resistor furnace under argon atmosphere. In these cases, the heating stage will be disregarded compared to isothermal stage.

Characterization

Global softening kinetics was followed by microhardness HV1 measurements in the centre of a transverse section of the rod. This softening is the result of two competing phenomena: recovery, which is active from the start of the annealing treatment and recrystallization that begins after an incubation time.

The grain structure was revealed by a tint etchant (containing 110ml H_2O, 12ml H_2SO_4, 4ml HF and 0.1ml HNO_3) used at 70°C. Observation at the optical microscope, under polarized light, allows one to discriminate between recovered grains and recrystallized ones, and to determine the incubation time.

For magnetic characterization, toroids of square cross sections 3x3mm were machined from the wire after tensile deformation, in order to avoid macroscopic demagnetizing field. Annealing treatment is directly performed on the toroid. The toroid is then fitted with a primary coil of n_1 turns to which the magnetizing current is fed and with a secondary coil of n_2 turns. Excitation field is measured via V1 using Ampere's theorem, and induction is obtained by numerical integration of the voltage V2 induced by the flux change (Faraday law) [3]. The samples were driven through hysteresis cycles at frequencies from 0.1 to 400Hz for peak induction around 1T, using the apparatus presented Figure 2.

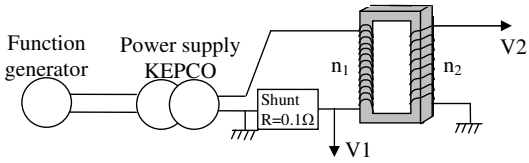

Figure 2. Scheme of the fluxmetric measurement system.

Results

Softening Kinetics

Evolution of hardness for different annealing time at 750 and 850°C is shown in Figure 3, for both grades. At 750°C, only recovery occurs. At 850°C, incubation time for recrystallization is represented by the arrow. The kinetics of both grades are very similar at 750°C when recovery is the only process involved, but show significant differences at 850°C when recrystallization takes place.

Recrystallization

Recrystallization is much slower in 430 than in 430Nb:

- The onset is considerably delayed for 430. At 850 °C, recrystallization starts after 3min for 430Nb and after 30min for 430.
- A sluggish recrystallization behavior is noted for 430: even 16h after the onset of recrystallization, deformed grains are still visible. These grains will be called island grains because they are surrounded by recrystallized areas. For 430Nb, recrystallization is complete after 10 min and no island grain is seen.

From a microstructural point of view, recrystallization leads for both grades to a large increase in the grain size (from 25µm to about 200µm) but the morphology of recrystallized grain are clearly different (see Figure 4). In 430Nb, rather equiaxed grains are formed during recrystallization whereas in 430 they have odd shapes with elongated branches.

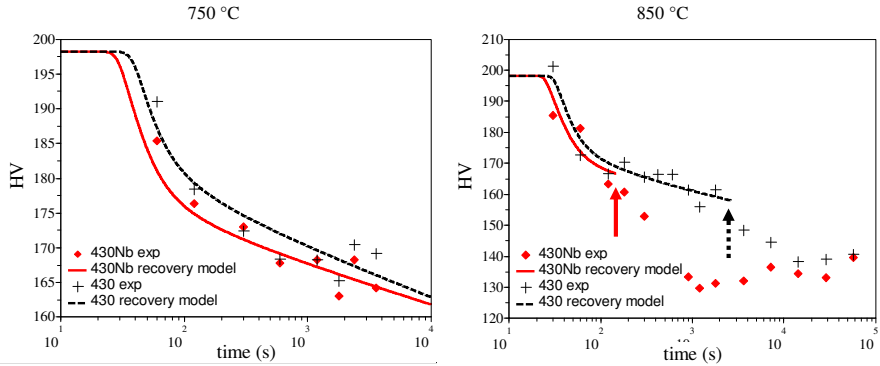

Figure 3. Softening kinetics at 750°C and 850°C determined experimentally. Recovery data (before the arrow) is fitted by Verdier's model with a good agreement [4].

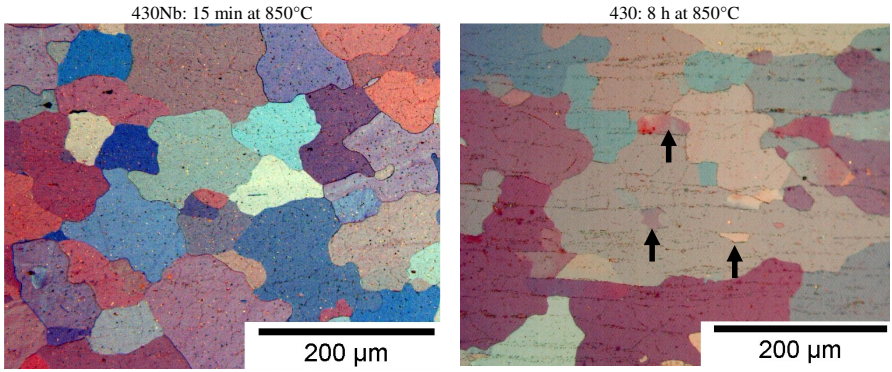

Figure 4. Optical micrographs of advanced recrystallization states revealed by a tint etchant. 430Nb: grains are equiaxed after complete recrystallization. 430: two populations can be distinguished: large recrystallized grains with odd shapes and 'island grains' having initial grain size 30µm (arrows).

Losses

Volumic energy loss per cycle is given by the area of the hysteresis loop B(H). One can notice from Fig. 5a, that dissipation at given peak induction is rate dependent and increases when magnetization frequency increases. However losses are also microstructure dependent, as

presented Figure 5b. Two largely different microstructures were selected: 430Nb in the deformed state and 430Nb after complete recrystallization (30min at 850°C). At low frequency, the recrystallized microstructure is more efficient to limit losses, whereas above 550Hz, the deformed state will be preferred. As a consequence, the frequency is a significant parameter to take into account for microstructure design.

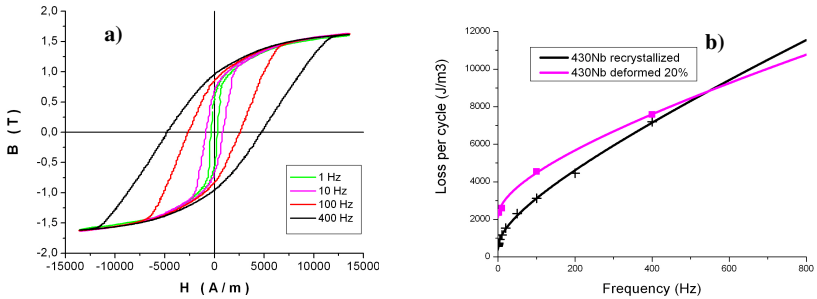

Figure 5. (a) Hysteresis loops for 430Nb in recrystallized state at different magnetization frequency and B_{max}=1.6 T. (b) Evolution of losses per cycle with frequency for two microstructures at B_{max}=1 T; experimental points were fitted by a classical law of the form: $P = a + bf + c\sqrt{f}$ *[3].*

Interpretation

Recovery Model

Before the onset of recrystallization, the softening kinetics can be described by the dislocation based model of recovery, developed by Verdier et al. [4]. In this model, the kinetic equation for dislocation density ρ decrease is given by Eq. 1 in which, b is the Burgers vector modulus, E(T) and μ(T) [5] are temperature dependent Young's modulus and shear modulus, M is the Taylor factor, α the interaction coefficient, υ_D the Debye frequency, k the Boltzmann constant, U_0 and ν are activation energy and volume.

$$\frac{d\rho}{dt} = -\frac{4\,b\,E(T(t))\,\upsilon_D}{M^2\,\alpha\,\mu(T(t))}\,\rho^{3/2}\,\exp\left(-\frac{U_0}{k\,T(t)}\right)\sinh\left(\frac{M\,\alpha\,\mu(T(t))\,b\,\sqrt{\rho}}{k\,T(t)}\,\upsilon\right). \qquad (1)$$

Eq. 1 was numerically solved under non-isothermal conditions, using the T(t) relationship determined experimentally, that takes into account sample heating stage.

Calibration of the model through activation parameters was done on hardness measurement before the recrystallization onset (see Figure 3). In this attempt, the hardness measurements were related to corresponding dislocation densities via the Taylor law. This work-hardening law is known to be valid for BCC iron at room temperature [6] and was assumed to remain valid for BCC stainless steels. Finally, activation parameters of Eq. 1 were adjusted on the corresponding

dislocation densities with a Levenberg-Marquardt optimization method. Good correlation was obtained with the following parameters:

- For 430: U_0 = 330 KJ.mol^{-1} and ν = 49 b^3
- For 430Nb: U_0 = 360 KJ.mol^{-1} and ν = 66 b^3

Activation energies are found to be rather close to self diffusion activation energy Q = 215KJ.mol^{-1} [7], leading to the conclusion that diffusive processes are involved during recovery. To conclude, it can be noticed from Fig. 3 that the model gives an accurate description of the softening kinetics for short time treatments (<2min) that are strongly non-isothermal as well as for long time treatment (>5min) for which the logarithmic decrease of HV is clearly noticed.

Comments on Recrystallization

Delay in recrystallization onset as well as 'sluggish' behaviour noticed in 430 (when compared to 430Nb) can both be considered as an effect of the precipitates location. It is quite well settled that for an IF steel after a low cold deformation, bulging on an existing grain boundary (SIBM) is the prevailing nucleation mechanism [8]. Nucleation occurs if the free length for bulging is larger than the critical radius r* to overcome capillarity effects; r* has an inverse dependence with the pressure ΔP acting on the grain boundary.

Two cases can be distinguished, depending on the distance between precipitates Λ along the boundary:

- If few precipitates are in the grain boundary $\Lambda >> 2r^*$, the free length for bulging is then the subgrain size d_{sg} [9].
- If intense precipitation takes place in the grain boundary, the free length for bulging is given by the minimum between d_{sg} and Λ.

In the latter description, the three characteristic lengths Λ, d_{sg} and r* are increasing during annealing but at different rates, respectively imposed by the stored energy decrease in each grain due to recovery, subgrain growth and precipitates coarsening.

TEM characterizations, not presented here, gave us some evidence that for 430Nb, $\Lambda >> 2r^*$ and nucleation is imposed by subgrain growth, whereas for 430, $\Lambda < d_{sg}$, leading to a nucleation imposed by precipitates coarsening. When precipitates are interacting with SIBM, the first nucleation is followed by growth in the deformed grain, but as soon as another grain boundary is reached, a re-nucleation criterion has to be fulfilled again for growth to continue (the critical size for re-nucleation is expected to be lower than for the first nucleation step because the pressure on the boundary is higher [10]). As a consequence of re-nucleation, growth direction will be highly anisotropic leading to odd shapes for recrystallized grains, as observed for 430. In this approach 'island grains' are deformed grains for which the distance between precipitates all around the boundary is too small for re-nucleation to occur.

Comments on Magnetic Losses

Losses are often considered as a sum of three contributions: $P = P_{hyst} + P_{cl} + P_{ex}$. The classical eddy-current energy losses per cycle (P_{cl}) depend on geometry, peak induction, resistivity and

frequency, whereas the two other contributions hysteresis losses (P_{hyst}) and excess losses (P_{ex}) are in addition microstructure dependent. P_{hyst} represents the total losses under quasistatic conditions and features the same microstructure dependence than coercive field Hc. In other words, defects experienced by a moving domain-wall are responsible of the macroscopic counter field Hc as well as the resulting energy dissipation P_{hyst}. Excess losses term is due to the spatial distribution of eddy-currents associated to domain walls displacements, strongly different from the distribution associated to classical approximation. Depending on microstructure, moving walls are considered as independent (case of GOSS textured materials) or as global "Magnetic Objects" (MOs) if strongly correlated (case of materials investigated here). The amplitude of excess losses is strongly related to the number of moving MOs, this parameter depending on microstructure too. Grain size d is the main microstructural parameter whose effect has been studied for both contributions. Hysteresis losses term decreases as 1/d whereas excess losses increases as $\sqrt{d.f}$ leading to an optimum grain size depending on frequency f [11]. For 430Nb, recrystallization leads to a large increase of grain size. Considering only this micro-structural aspect, the detrimental effect of recrystallization on magnetic losses, noticed experimentally at high frequency, can be well understood.

430LNb – A New Ferritic Wire for Automotive Exhaust Applications

Materials and Experimental Procedure

Materials

The 430LNb wire was used to weld AISI 409, 441 and 436 sheets and was compared with 308LSi and 307Si filler materials. A comparison in terms of weldability was also made with a 409Cb wire, used to weld AISI 409. The chemical analysis of the wires and sheets evaluated are given in Table 2 below.

Table 2. Chemical analysis of the welding wires and sheets (wt.%).

Sheets	**C**	**Si**	**S**	**P**	**Mn**	**Ni**	**Cr**	**Mo**	**Ti**	**Nb**	**N**
409	0.007	0.5	0.004	0.021	0.2	0.1	11.2	0.01	0.18	-	0.010
436	0.040	0.4	0.004	0.022	0.5	0.1	17.2	1.20	-	0.54	0.024
441	0.014	0.5	0.003	0.020	0.5	0.2	17.5	0.02	0.15	0.55	0.018
Wires	**C**	**Si**	**S**	**P**	**Mn**	**Ni**	**Cr**	**Mo**	**Ti**	**Nb**	**N**
307Si	0.077	0.7	0.009	0.016	7.1	8.3	18.9	0.12	-	-	0.056
308LSi	0.014	0.9	0.008	0.018	1.8	10.3	19.9	0.11	-	-	0.045
409Nb	0.056	1.3	0.017	0.020	1.6	0.2	12.2	0.06	0.36	0.93	0.037
430LNb	0.017	0.4	0.002	0.018	0.3	0.3	18.0	0.04	0.01	0.32	0.017

Welding Procedure

In order to enable mechanical testing of the welds, gapless MIG butt welding was performed. The welding parameters were adapted to comply with standard exhaust system welding procedures. The same welding parameters were used for all the welding wires tested: 308LSi,

307Si, 409Cb and 430LNb. Figure 6 shows an example of the weld seams obtained (441/441 assembly with a 430LNb wire).

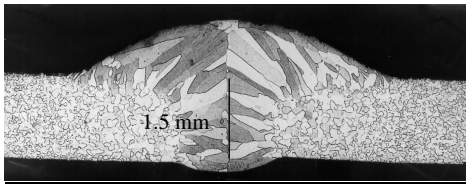

Figure 6. 441/441 assembly produced with a 430LNb wire.

Intergranular Corrosion Test

20mm wide specimens with a central weld, cut from the AISI 436 and 441 assemblies, were subjected in the as welded condition to the ASTM A262-E test. In the case of AISI 409 assemblies, the "modified" ASTM A262-E test [12] was employed.

Dip-Dry Tests

A specific "dip-dry" test has been developed, illustrated in Figure 7, which involves the following cyclic procedure:

- Periodic immersion into solutions carefully selected to simulate exposure to condensates or saline splashing, in order to reproduce wet corrosion mechanisms;
- Transfer to a furnace simulating high speed running and the associated high temperature corrosion and oxidation mechanisms.

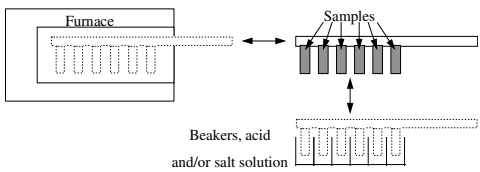

Figure 7. Dip-dry test: alternate immersion in a solution and exposure in a furnace.

Thermal Fatigue

A special thermal fatigue test has been developed to evaluate the thermal fatigue resistance of stainless steel sheets. The testing rig and the experimental procedure are described in detail in references [13] and [14]. In summary, thermal cycles are imposed on a clamped V-shaped specimen, by alternate resistance heating and air cooling (Figure 8). Damage accumulation at the top of the V due to the thermally-induced plastic strain eventually leads to failure of the

specimen. The thermal fatigue life of the specimen is expressed as the number of cycles to failure and depends on the maximum and minimum temperature during the thermal cycle, the specimen thickness, and the material concerned. The thermal cycle is defined by a maximum temperature of 900°C and a minimum temperature of 250°C, with no holding time. The duration of each cycle is about 200 seconds. The thickness is kept constant and equal to 1.5mm, 3 or 4 specimens being tested for each type of welding wire. Homogeneous 441, 409 and 436 assemblies produced with the different welding wires were compared.

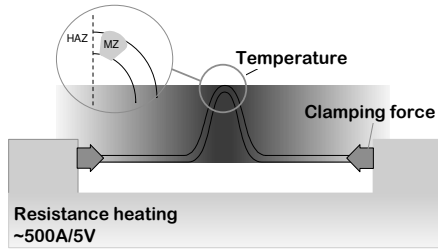

Figure 8. Schematic principle of the thermal fatigue test.

Results and Discussion

Weldability and Basic Properties of the Weld Seams

Weldability, in terms of fluidity, wetability and ease of execution, was essentially the same for all the welding wires tested. In contrast, large differences were observed in the microhardness of the weld seams:

- With austenitic filler metals, there is a sharp discontinuity in hardness between the fusion zone and the ferritic base metal (cf. example hardness profiles for 409/409 and 441/441 assemblies in Figure 9: this is due to extensive martensite formation in the melted zone, especially in the 409/409 assembly;
- With ferritic filler metals, especially 430LNb, the hardness of the fusion zone is the same as that of the base metal.

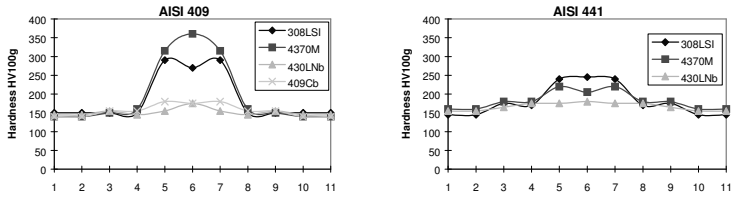

Figure 9. Hardness profiles on 409/409 and 441/441 assemblies (1.5mm thick sheet) made with different welding wires (4370M = 307Si)

.

Intergranular Corrosion Resistance

None of the assemblies tested (AISI 409, 441 and 436, with 430LNb, 308LSi and 307Si filler metals) showed any sign of intergranular corrosion [15].

Dip-Dry Tests

In the temperature range studied (furnace temperatures of 300°C-800°C), no significant difference in corrosion resistance was revealed between assemblies produced with 430LNb wire and those made with austenitic filler metals, whatever the corrosive medium, either synthetic condensate (internal parts) or salt solution (external parts). Figure 10 shows an example of a specimen after testing.

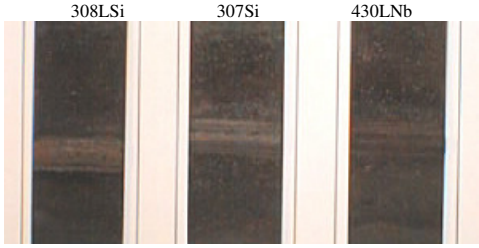

Figure 10. Dip-dry test (urban cycle-synthetic condensate-600°C-30 days) on 441/441 assemblies.

Thermal Fatigue

Figure 11 shows the results of thermal fatigue lives obtained for 308LSi, 307Si and 430LNb wires used for welding of 409/409 and 441/441 assemblies. The fatigue lives are expressed by the ratio of the life of welded specimens over the life of the base metal. 409 specimens welded using the 430LNb wire exhibits very good thermal fatigue resistance compare to specimen welded using 308LSi and 307Si wires.

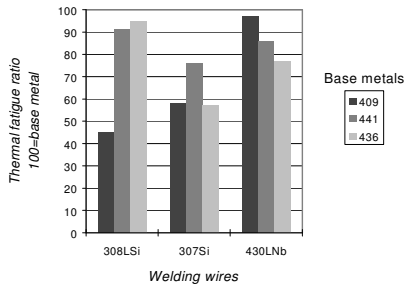

Figure 11. Thermal fatigue lives for 409, 436 and 441 assemblies produced with 307Si, 308LSi and 430LNb welding wires, expressed as a percentage of the lives for the unwelded base metals.

In the case of 441 and 436 assemblies, the fatigue thermal life of the specimen welded with 430LNb wire is always included in the range of lives of specimen welded using 308LSi and 307Si (see Figure 11). Metallographic observations evidence two type of thermal fatigue crack propagation in specimen : in Heat Affected Zone (HAZ) or Base Metal (BM) or at interface between HAZ and Fusion Zone (FZ), as shown in Table 3 and Figure 12.

Table 3. Area of thermal fatigue cracks.

Welding wires / **Base metals**	**308LSi**	**307Si**	**430LNb**
409	❍	×	❍
441	×	×	❍
436	×	×	❍

× indicates a crack at interface between Heated Affected Zone and Fusion Zone;
❍ indicates a crack in Heated Affected Zone or Base Metal.

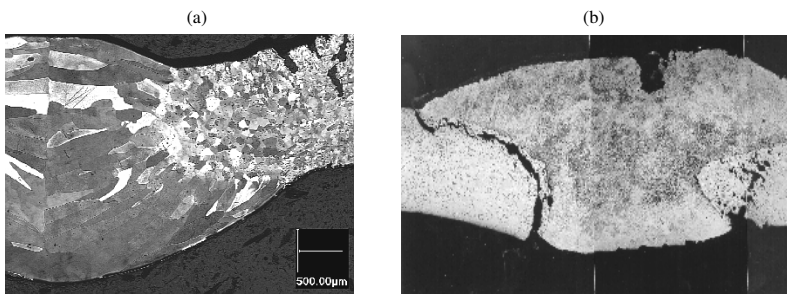

Figure 12. Thermal fatigue cracks: (a) 441 assembly welded with 430LNb (crack in base metal/HAZ, ❍); (b) 441 assembly welded with 307Si (crack at interface HAZ/FZ, ×).

The low resistance obtained for the assemblies welded with 307Si wire can be explained by a systematic fatigue crack propagation occurring at the interface between the melting zone and the heat affected zone. In case of 409 assemblies the advantage of durability for the ferritic welding wire is more evident. We can notice a larger plastic strain of the melting zone in case of austenitic wires due to a higher thermal expansion coefficient compared to ferritic base metals, and which can lead to a thermally-induced deformation of the exhaust component near the welded seam (catalytic converter, manifold).

Tests Carried Out on Real Exhaust Components

Within the framework of a partnership with Faurecia, a major exhaust system manufacturer, MIG welding tests using both 430LNb wire and 308LSi wire for comparison have been carried out on different assembly configurations, two of which are shown in Figure 13.

The behaviour of the two filler wires is very similar. In particular, the welding parameters are fairly close, with a slightly higher welding current for 430LNb, probably due to a difference in electrical conductivity. In the tests on the racetrack converter can, somewhat higher welding speeds were found to be possible with 430LNb wire.

Figure 13. Fillet welds on Faurecia catalysts: (a) straight weld on an AISI 409 racetrack type catalytic converter can; (b) circular weld on an AISI 441 cylindrical catalytic converter can.

Conclusions

Usually niobium is added in ferritic stainless steels to avoid chromium carbides precipitation and then to improve corrosion resistance and to avoid embrittlement. This work shows that niobium can also be used in ferritic stainless steels long products to improve other metallurgical properties that can be very useful for the automotive industry.

Low niobium stabilization is changing completely the carbides and nitrides precipitates location from intergranular to homogeneous distribution. This greatly facilitates the recrystallization process and the incubation time for recrystallization is significantly lowered. A SIBM nucleation in interaction with precipitates can explain qualitatively these differences in softening kinetics, as

well as the difference in grain morphology. Moreover, magnetic losses have been shown to be microstructure sensitive and 17%CrNb ferritic stainless steels is a very interesting solution for actuation when soft magnetic properties are required.

Nb stabilization in ferritic stainless steels improves also corrosion resistance to salt attack, cyclic oxidation and thermal fatigue resistance of the weld in the case of a welding filler wire for the exhaust line.

Specific tests to the automotive exhaust application have been undertaken in the laboratory in order to compare the service behavior of welds produced using 430LNb wire with that of similar welds obtained with austenitic filler metals. These included dip-dry corrosion-oxidation tests simulating the combination of salt attack and high temperature corrosion, and thermal fatigue tests involving cycling of restrained specimens between 250 and 900°C. All the results obtained confirm that the 430LNb welding wire is at least as good as the austenitic filler materials most commonly employed in Europe, and sometimes better. Finally, tests carried out on real components by exhaust system manufacturers also confirm the high productivity and good quality of the welds.

References

1. K. Ara: *IEEE Transactions on Magnetics,* Vol. 25 (1989), p.2617.

2. M. Mantel, B. Baroux, D. Gex and P. Pedarre, Recrystallization '90, edited by T. Chandra, The Minerals, Metals & Materials Society (1990), p.345.

3. O. Geoffroy, in: Techniques de l'Ingénieur, edited by T.I. Sciences et Techniques, volume D2080 (2006).

4. M. Verdier, Y. Bréchet and P. Guyot, *Acta Mater.* Vol. 47 (1999), p.127.

5. M. Rouby and P. Blanchard, in Les aciers inoxydables, edited by P. Lacombe, EDP (1990).

6. E. Rauch, HDR Thesis, INPG (1993).

7. S.P. Ray and B.D. Sharma, *Acta Metallurgica*, Vol. 16 (1968).

8. H. Réglé, HDR Thesis Université Paris 13 (2005).

9. J. Dunlop, PhD Thesis, INPG (2005).

10. P. Bate and B. Hutchinson, *Scripta Materialia,* Vol. 36 (1997), p.1995.

11. M.F. de Campos, T. Yonamine, M. Fukuhara, F.J.G. Landgraf, C.A. Achete and F. P. Missell, *IEEE Transactions on Magnetics,* Vol. 42 (2006).

12. T.M. Devine and J. Drummond, 'An Accelerated Intergranular Corrosion Test for Detecting Sensitization in Low Chromium Ferritic Stainless Steel', *in Corrosion NACE*, 38 (6), 1982.

13. H. Sassoulas, P-O. Santacreu, *18ème Journée de Printemps de la SF2M- Dimensionnement en Fatigue des Structures : Démarche et outils*, Paris, 2-3 June 1999, p.161.

14. P-O. Santacreu et al, *Thermal Stresses'99*, Cracow, Poland, June 13-17 1999, p.245.

15. N. Renaudot et al., SAE 2000 World Congress, Detroit, Michigan, March 6-9 (2000).